CrossMark

Influence of Ca^{2+} ions substitution on structural, microstructural, electrical and magnetic properties of $Mg_{0.2-x}Ca_xMn_{0.5}Zn_{0.3}Fe_2O_4$ ferrites

Rumana Maleque[1] · Md. D. Rahaman[1] · A. K. M. Akther Hossain[2]

Abstract Mg–Ca–Mn–Zn ferrites having general formula $Mg_{0.2-x}Ca_xMn_{0.3}Zn_{0.5}Fe_2O_4$ (x = 0, 0.10, 0.15 and 0.20) were synthesized using solid state reaction method and sintered at 1100 and 1200 °C for 4 h. Structural, microstructural and elemental analyses of synthesized ferrites were performed by X-ray diffraction (XRD), Fourier transform infrared (FTIR) spectroscopy, scanning electron microscopy (SEM) and energy dispersive analysis of X-ray. A cubical spinel crystal structure with secondary phases is conformed in synthesized samples by XRD analysis. The lattice parameter decreased initially and then increases at x = 0.20 at 1100 °C. On contrary, the lattice parameter increases with Ca^{2+} ions concentration at 1200 °C which is attributed due to the different ionic radius of Mg^{2+} and Ca^{2+} ions. The FTIR spectra show the presence of high frequency and low frequency band at 559.36–460.14 cm^{-1} at 1100 °C and 549.71–558.35 cm^{-1} at 1200 °C corresponding to the tetrahedral and the octahedral sites. The SEM images revealed that the average grain size increases with the increase of Ca^{2+} ions concentration which may be attributed due to the fact that Ca^{2+} ions influences the microstructure by forming a liquid phase during sintering process and expedites the grain growth by lowering the rate of cation interdiffusion. Low frequency dielectric dispersion is consistent with the Maxwell–Wagner interfacial polarization. Dielectric constant increases with Ca^{2+} concentration for both sintering temperatures. The samples x = 0.10 and 0.15 exhibits highest conductivity at 1100 and 1200 °C, respectively because the electron hopping between Fe^{3+} and Fe^{2+} ions increases. The conduction process is attributed due to the presence of grain and grain boundary effect as revealed by the impedance study. The significant decrement in permeability with Ca^{2+} concentration is attributed due to the lower saturation magnetization and increased inner stress or crystal magnetic anisotropy.

1 Introduction

In due course of time, it is necessary to synthesize of polycrystalline ferrites through different synthetic routes with diverse properties to meet the requirements of today's technological demands [1, 2]. Among the ferrites, Mg–Mn–Zn ferrites are the important ferrites because they possess moderate initial permeability, high electrical resistivity and relatively easy synthesizing method and due to their wide applications in magnetic cores and deflection yokes in communication, deflection yoke core for high-resolution display monitors, electronic equipment and domestic appliances [3–7]. It is reported that the replacement of nonmagnetic ion of Mg^{2+} by magnetic ion of Mn^{2+} (L = 0, S = 5/2, J = 5/2) in Mg–Zn ferrites affect the magnetic properties because the substitution of Mn^{2+} ions can reduce the magnetic coercivity since the angular momentum is Mn^{2+} ions is zero (L = 0). In spinel lattice, Mn^{2+} cations are at its high spin state (S = 5/2). The Mn^{2+} cations affect the saturation magnetization since it has 5d electron configurations ($e^2t_2^3$ and $t_{2g}^3e_g^2$) at the tetrahedral and octahedral lattice site [8, 9]. Rikukawa et al. have studied low temperature sintering of magnesium–manganese–zinc ferrite [10]. Gorelik

✉ Md. D. Rahaman
   dalilurrahaman1976@gmail.com

1 Department of Physics, University of Dhaka, Dhaka 1000, Bangladesh

2 Department of Physics, Bangladesh University of Engineering and Technology (BUET), Dhaka 1000, Bangladesh

et al. have reported the aging mechanism in magnesium–manganese–zinc ferrite [11]. On the other hand, Ebrahimi et al. have investigated the optimum condition for the preparation of pure magnesium–manganese–zinc ferrite [12]. Fan et al. have studied the sintering temperature dependent properties of magnesium–manganese–zinc ferrite [13]. The mechanism of the initial permeability in magnesium–manganese–zinc ferrite has studied by Kolenbrander et al. [14]. Van der Zaag et al. have studied the effect of intragranular domain walls in magnesium–manganese–zinc [15]. It has been reported in the literature that the substitution of non-magnetic divalent ions in ferrites could enhance the physical, electrical, and magnetic properties as well as improve the quality of material for practical applications [16]. For high frequency applications, it is necessary to study the frequency dependent electrical, dielectric and magnetic properties. It is reported that the physical, electrical and magnetic properties of polycrystalline ferrites are dependent on sintering composition, synthesis method, microstructure, dwell time, heating and cooling rate, nature and amount of dopant, cations distribution and particle size [17, 18]. In the spinel lattice, certain amount of Ca^{2+} ions can occupy [19]. It has been reported that the maximum 23% of Ca^{2+} ions can be substituted for Mg^{2+} ions in magnesium ferrite [20]. Several research works have been performed to evaluate the electrical, magnetic properties and thermal coagulation therapy in ac magnetic field of Ca^{2+} substituted spinel ferrites such as $Ni_{0.245}Zn_{0.755}Fe_2O_4$ [19], $Ni_{0.5}Cu_{0.3}Zn_{0.2}Fe_2O_4$ [21], Ni–Zn–Ca [22], $Mg_{1-x}Ca_xNi_yFe_{2-y}O_4$ [23], $Mg_{1-x}Ca_xFe_2O_4$ [20, 24], $Cd_{0.5}Mg_{0.5-x}Ca_xFe_2O_4$ [25], and $Mg_{0.2}Ca_{0.8}Fe_2O_4$ [26]. In our previous study, we report the sintering temperature dependent 10% Ca-doped $Mn_{0.6}Zn_{0.4}Fe_2O_4$ [27]. Based on the literature survey, it can be assumed that Ca^{2+} substitution modify the electric and magnetic properties of ferrites considerably. The occupancy of Ca^{2+} into the spinel lattice would create a lattice distortion due to its larger ionic radius. As results, the modification of material properties to an appreciable extent is expected. There are no studies available in the literature on the influence of Ca^{2+} ions substitution on the structural, microstructural and electromagnetic properties of $Mg_{0.2}Mn_{0.3}Zn_{0.5}Fe_2O_4$ ferrite. It would be interesting to substitute a large cation such as Ca^{2+} for Mg^{2+} in $Mg_{0.2}Mn_{0.5}Zn_{0.3}Fe_2O_4$ ferrite because the ionic radius of the cations involved are Mg^{2+} (0.72 Å), Mn^{3+} (Å), Mn^{4+} (0.52 Å), Ca (1.14 Å), Zn (0.68 Å) and Fe^{3+} (0.67 Å) at A-site and B-site are 0.49 and 0.64 Å. The objectives of the present work are to study the effect of Ca^{2+} ions substitution on structural, microstructural, electrical and magnetic properties of $Mg_{0.2}Mn_{0.5}Zn_{0.3}Fe_2O_4$ ferrite. In the present study, the study of dielectric constant, dielectric loss, ac electrical conductivity and complex permeability are made

for $Mg_{0.2-x}Ca_xMn_{0.5}Zn_{0.3}Fe_2O_4$ (x = 0.0, 0.10, 0.15, and 0.20) ferrites, which makes better understanding the impact of Ca^{2+} on the electrical conduction mechanism, dielectric polarization and complex permeability.

2 Experimental

2.1 Synthesis of materials

Mg–Ca–Mn–Zn ferrites having general formula $Mg_{0.2-x}Ca_xMn_{0.3}Zn_{0.5}Fe_2O_4$ (x = 0, 0.10, 0.15 and 0.20) ferrites powder were synthesized by solid state reaction method using MgO (≥99.9%), $CaCO_3$ (≥99.9%), $MnCO_3$ (≥99.9%), ZnO (≥99.9%) and Fe_2O_3 (≥99.9%) as a raw materials. The raw materials were mixed in stoichiometric proportions and ground for 4 h. Then the mixed powders were calcined at 900 °C for 5 h with the heating and cooling rates at 10 and 5 °C/min, respectively. The calcined powders were ground again with a pestle in an agate mortar for making fine powder. Powders were pressed into pellet-shaped and toroidal samples with a uniaxial pressure of 6400 psi with polyvinyl alcohol (PVA) as binder. Finally, the samples were sintered at 1100 and 1200 °C for 4 h with the same heating and cooling rates as that of calcination process.

2.2 Characterization

Crystal structure study was performed using Rigaku Ultima IV (Japan) using X-ray powder diffractometer (RIGAKU Ultima IV, Japan). The infrared absorption spectra were carried out by an infrared spectrophotometer (Shimadzu FTIR 8400S). The crystallite size was calculated by the Debye–Scherrer's formula [28]. The lattice constant (a) was calculated by using d_{hkl} spacing and *hkl* parameters by using: $a = \frac{\lambda[h^2+k^2+l^2]^{1/2}}{2\sin\theta}$, where *hkl* are the Miller indices of the crystal plane [29]. Hopping length of octahedral site (L_B) and tetrahedral (L_A) were determined using: $L_A = \frac{a\sqrt{3}}{4}$ and $L_B = \frac{a\sqrt{2}}{4}$, respectively [30]. The value of the tetrahedral radii (R_{tetra}) and the octahedral radii (R_{octa}) is calculated by $R_{tetra} = a\sqrt{3}(u-0.25) - R_0$ and $R_{octa} = a\left(\frac{5}{8}-u\right) - R_0$ respectively, where *a* is lattice parameter, *u* is oxygen positional parameter, R_0 is the radius of oxygen ion (1.32 Å) [31]. The value of oxygen parameter for an ideal FCC crystal is 0.375 [31]. The tetrahedral bond length $d_{AO}(d_{A-O^{2-}})$ and the octahedral bond length $d_{BO}(d_{B-O^{2-}})$ can be calculated using the relations: $d_{AO} = a\sqrt{3}(u-0.25)$ and $d_{BO} = a\left(3u^2 - \frac{11}{4}u + \frac{43}{64}\right)^{1/2}$ [32]. The tetrahedral edge d_{AE} and the octahedral edge d_{BE}

and unshared edge d_{BEU} can be determined using the relations: $d_{AE} = a\sqrt{2}(2u - 0.5)$, $d_{BE} = a\sqrt{2}(1 - 2u)$ and $d_{BEU} = a\left(4u^2 - 3u + \frac{11}{16}\right)^{1/2}$ [32]. The morphology and elemental analysis were characterized by scanning electron microscopy (SEM) (Model: JEOL-JSM-6490LA) equipped with energy dispersive X-ray spectrophotometer (EDAX). The average grain size was calculated according to Rahaman et al. [27]. X-ray density (ρ_x), bulk density (ρ_B) and porosity were obtained based on the available literatures [33]. Electrical and magnetic properties were carried out by Wynne Kerr impedance analyzer (Model: 6500). The real part (Z') and the imaginary part (ε'') of complex impedance were determined using: $Z' = \frac{G}{G^2 + \omega^2 C_p^2}$ and $Z'' = \frac{\omega C_P}{G^2 + \omega^2 C_P^2}$ relations [34]. The initial permeability of the samples was calculated according to Rahaman et al. [27].

3 Results and discussion

3.1 X-ray diffraction analysis

Figure 1a, b show the X-ray diffraction spectra of $Mg_{0.2-x}Ca_xMn_{0.5}Zn_{0.3}Fe_2O_4$ (x = 0.0, 0.10, 0.15 and 0.20) ferrites at 1100 and 1200 °C, respectively. The XRD patterns confirm the formation of a cubic spinel structure. It is observed that secondary phases appeared in the XRD patterns of $Mg_{0.2}Mn_{0.5}Zn_{0.3}Fe_2O_4$ at 1100 °C which is attributed due to the hematite (α-Fe_2O_3). The possible reason for the appearance of secondary phase in $Mg_{0.2}Mn_{0.5}Zn_{0.3}Fe_2O_4$ sintered powder is that the solid state reaction was not completed under the sintering process at 1100 °C. Hematite (α-Fe_2O_3) phase is completely disappeared in $Mg_{0.2}Mn_{0.5}Zn_{0.3}Fe_2O_4$ ferrite at 1200 °C which means that the $Mg_{0.2}Mn_{0.5}Zn_{0.3}Fe_2O_4$ was considered to be pure single-phase spinel structure. The impurity phases appeared in the Ca^{2+} substituted samples at 1100 and 1200 °C are attributed due to $Ca_2Fe_2O_5$ or $CaFe_2O_4$ [19, 21, 24]. In Table 1, the lattice parameters for the samples sintered at 1100 and 1200 °C are presented. At 1100 °C, the lattice parameter increases up to x = 0.15 and then decreases for x = 0.20. On the other hand, the lattice parameter increases with Ca^{2+} concentration at 1200 °C. The little increase in the lattice parameter in the Ca^{2+} substituted samples is attributed to the differences of the ionic radii of Ca^{2+} and Mg^{2+}. Ca^{2+} has larger ionic radius (1.14 Å) as compared to Mg^{2+} (0.66 Å). The substitution of Ca^{2+} leads to the expansion of $Mg_{0.2}Mn_{0.5}Zn_{0.3}Fe_2O_4$ lattice. As a consequence, the lattice constant increases. A slight decrease in the lattice constant for x = 0.20 is due to the migration of few Mg^{2+} to A-sites owing to the incorporation of Ca^{2+} on the B-sites. The decrease in lattice
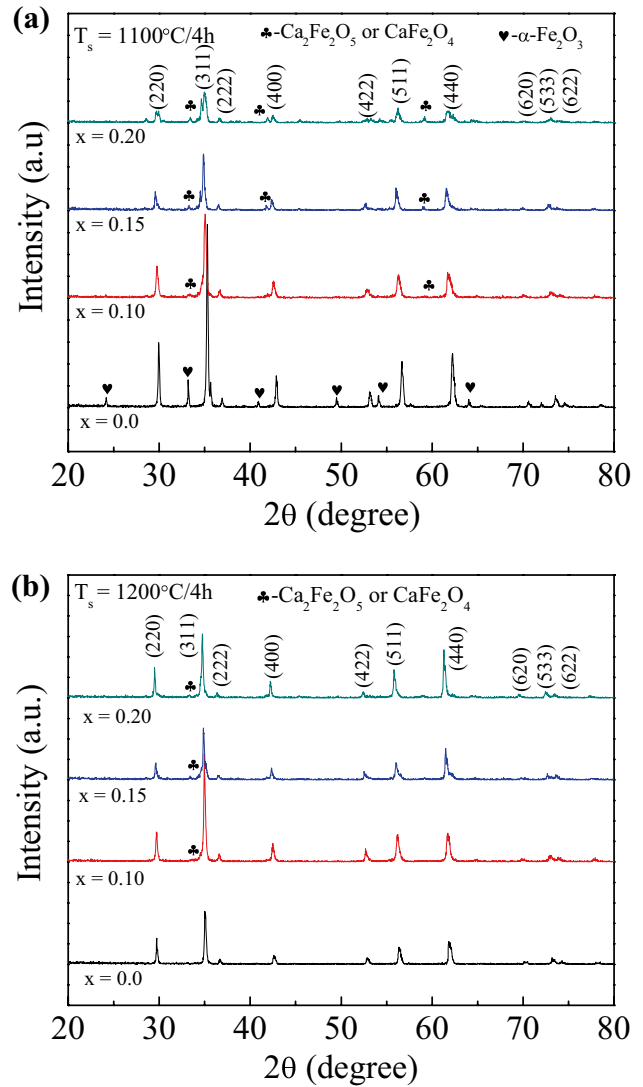

Fig. 1 XRD patterns of $Mg_{0.2-x}Ca_xMn_{0.5}Zn_{0.3}Fe_2O_4$ (x = 0.0 0.10, 0.15, and 0.20): sintered at **a** 1100 °C and **b** 1200 °C for 4 h, respectively

constant for x = 0.15 indicates the solubility limit. When the solubility limit is obtained no further Ca^{2+} is dissolved in $Mg_{0.2}Mn_{0.5}Zn_{0.3}Fe_2O_4$ lattice and Ca^{2+} ions accumulate at the grain boundaries and thus form the thin insulating layer around the grains. The existence of $Ca_2Fe_2O_5$ or $CaFe_2O_4$ phases on the grain boundaries suppresses the grain growth by hindering the mobility of grain boundary [19, 21, 24]. The Ca^{2+} may reside on B-sites as Ca^{2+} have larger ionic radius (1.14 Å) as compare to that of Fe^{3+} (0.64 Å) ions. The occupation probability of Ca^{2+} in the A-sites is very remote because the A-sites are too small for the occupation of large Ca^{2+}. When the Ca^{2+} ions occupy in B-sites, the internal stresses may occur in B-sites because of their large ionic radii [19, 21, 24]. The variation of lattice constant with sintering temperatures is attributed due to the variation

Table 1 Chemical composition, lattice parameter (a), the A- and B-site bond lengths (d_{AO} and d_{BO}), the tetrahedral edge (d_{AE}), the octahedral shared edge (d_{BE}) and octahedral unshared edge (d_{BEU}), tetrahedral hopping length (L_A) and octahedral hopping length (L_B) of various $Mg_{0.2-x}Ca_xMn_{0.3}Zn_{0.5}Fe_2O_4$ (x = 0, 0.0, 0.15, and 0.20) at different sintering temperatures (T_s) for 4 h

T_s (°C)	Composition (x)	a (Å)	R_{octa} (Å)	R_{tetra} (Å)	d_{AO} (Å)	d_{BO} (Å)	d_{AE} (Å)	d_{BE} (Å)	d_{BEU} (Å)	L_A (Å)	L_B (Å)
1100	0.0	8.4739	0.7985	0.5147	1.8347	2.1185	2.9960	2.9960	2.9960	3.6693	2.9960
	0.10	8.4895	0.8024	0.5180	1.8380	2.1224	3.0015	3.0015	3.0015	3.6751	3.0015
	0.15	8.5287	0.8122	0.5265	1.8465	2.1322	3.0154	3.0154	3.0154	3.6960	3.0154
	0.20	8.5083	0.8071	0.5221	1.8421	2.1271	3.0081	3.0081	3.0081	3.6842	3.0081
1200	0.0	8.4840	0.8010	0.5168	1.8368	2.1210	2.9995	2.9995	2.9995	3.6737	2.9995
	0.10	8.5003	0.8051	0.5204	1.8404	2.1251	3.0053	3.0053	3.0053	3.6807	3.0053
	0.15	8.5300	0.8125	0.5268	1.8468	2.1325	3.0158	3.0158	3.0158	3.6936	3.0158
	0.20	8.5552	0.8188	0.5323	1.8523	2.1388	3.0247	3.0247	3.0247	3.7045	3.0247

of cation distribution between both B-sites and A-sites. It is observed that the most intense (311) peak shifts towards the lower angle side with the increase of Ca^{2+} concentration at 1100 and 1200 °C, respectively which reveals the expansion of unit cell lattice due to Ca^{2+} substitutions. In Table 2, the crystallite size at 1100 and 1200 °C is presented. The crystallite size for $Mg_{0.2}Mn_{0.5}Zn_{0.3}Fe_2O_4$ sample is higher than that of Ca^{2+} substituted samples 1100 °C, which is attributed due to the fact that the Ca^{2+} restrict the grain growth of $Mg_{0.2}Mn_{0.5}Zn_{0.3}Fe_2O_4$. It is observed that the crystallite size of Ca^{2+} substituted samples is higher at 1200 °C than that of 1100 °C. Crystallite size increases with sintering temperature which is attributed due to the Oswald ripening. From Table 2, it is found that the grain sizes obtained from SEM are significantly larger than the crystallite sizes as determined by Debye–Scherer's formula at both sintering temperature. The difference between abovementioned matters is attributed due to the microstructures consisting of coalesced and multi-grained structures [20]. The hopping length between the magnetic ions in the A-site and in the B-site is calculated with the help of XRD

data and tabulated in Table 1. It is found that the hopping lengths (L_A and L_B) increase with increase of Ca^{2+} substitution which suggests that the magnetic ions go far away to each other. On the other hand, tetrahedral bond length $d_{AO}(d_{A-O^{2-}})$, the octahedral bond length $d_{BO}(d_{B-O^{2-}})$, tetrahedral edge d_{AE}, the octahedral edge d_{BE} and unshared edge d_{BEU} are calculated and presented in Table 1. Therefore, to the difference in the ionic radii of Ca^{2+} and Mg^{2+} ions, the allied parameters increases with the increase of Ca^{2+} ions.

3.2 Fourier transform infrared spectroscopic (FTIR) analysis

FTIR spectra of $Mg_{0.2-x}Ca_xMn_{0.5}Zn_{0.3}Fe_2O_4$ ferrites are shown in Fig. 2a, b sintered at 1100 and 1200 °C for 4 h, respectively. It is observed that the high frequency band ν_1 and low frequency band ν_2 are in the range of 559.36–549.71 and 464.84–458.35 cm^{-1} at 1100 and 1200 °C, respectively. Waldron [35] has reported that their presence and assigned the high frequency band ν_1 which is attributed due to the A-site where it is produced

Table 2 Values of FTIR vibrational wavenumbers (ν_1 and ν_2), volume of the cell (V_{cll}), bulk density (ρ_B), X-ray density (ρ_x), porosity (P), grain size and crystallite size for the most intense crystalline peak (311) (D_{311}), of various $Mg_{0.2-x}Ca_xMn_{0.3}Zn_{0.5}Fe_2O_4$ (x = 0, 0.0, 0.15, and 0.20) at different sintering temperatures (T_s) for 4 h

| T_s (°C)	Composition (x)	FTIR vibrational wavenumbers ν_1 (cm^{-1})	ν_2 (cm^{-1})	V_{cell} (Å³)	ρ_B (g/cm³)	ρ_x (g/cm³)	P (%)	Grain size (μm)	D_{311} (nm)
1100	0.0	559.36	460.99	608.4852	3.97	4.97	20	4.37	155
	0.10	545.85	460.14	611.8519	4.59	4.98	8	4.71	85
	0.15	542.00	462.61	620.3668	4.62	4.92	6	4.78	98
	0.20	538.14	464.84	615.9258	4.65	4.98	7	5.02	68
1200	0.0	549.71	458.35	610.6636	4.39	4.95	11	9.79	103
	0.10	534.28	458.65	614.1900	4.45	4.96	10	11.29	115
	0.15	532.35	459.40	620.6505	4.49	4.92	9	11.89	122
	0.20	522.33	460.14	626.1675	4.55	4.90	7	11.91	121
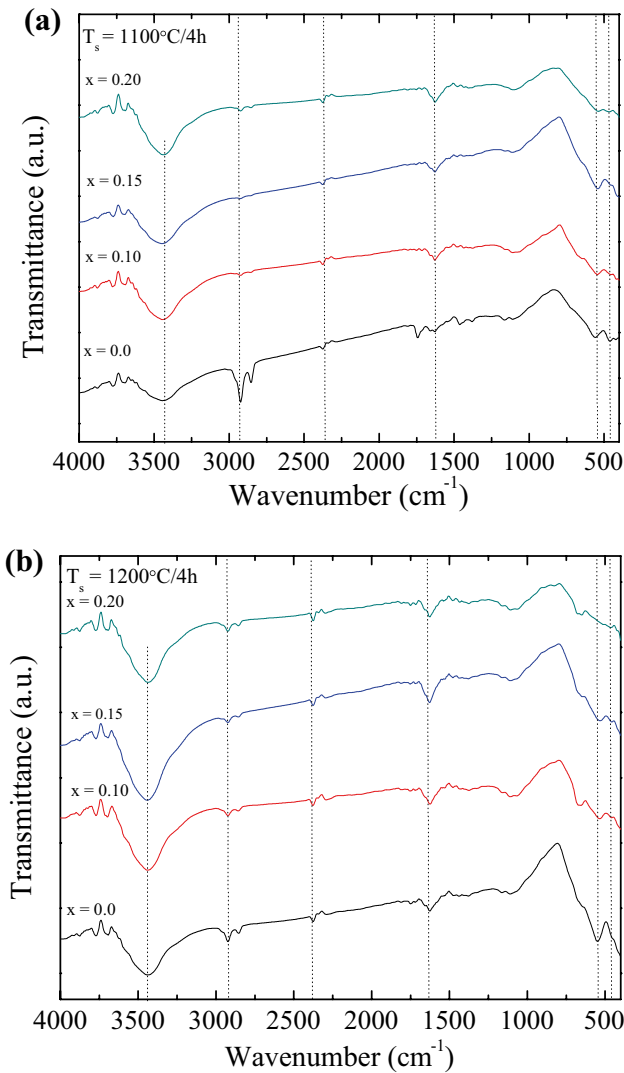
Fig. 2 FTIR patterns of $Mg_{0.2-x}Ca_xMn_{0.5}Zn_{0.3}Fe_2O_4$ (x=0.0 0.10, 0.15, and 0.20) sintered at **a** 1100 °C and **b** 1200 °C for 4 h, respectively

by stretching vibrations of A-site metal–oxygen bonding, and low frequency band v_2 which is attributed due to the metal–oxygen bonding in the B-sites. Due to the shorter bond length of the A-site cluster than that of the B-site cluster, the v_1 values are higher than those of v_2. The values of v_1 and v_2 at 1100 and 1200 °C are presented in Table 2. The spectra showed a small shift by the substitution of Ca^{2+} i.e. the A-site bands are shifted from higher value (559.36 cm^{-1}) to lower value (538.14 cm^{-1}) at 1100 °C. On the other hand, the A-site bands are shifted from higher value (549.71 cm^{-1}) to lower value (522.33 cm^{-1}) at 1200 °C. The shifting of v_1 and v_2 reconfirms the cation distribution in both B-sites and A-sites of the synthesized samples. The shift towards higher frequency can be attributed to the shifting of Fe^{3+} towards the

O^{2-}. The $Fe^{3+}–O^{2-}$ bond distance decreases since larger ionic radii of Ca^{2+} occupies A-site. Similarly, v_2 bands are slightly shifted to higher value i.e. 460.99–464.84 cm^{-1} at 1100 °C and 458.35–460.14 cm^{-1} at 1200 °C. The following bands appeared in the spectrum such as 1003.28 cm^{-1} (x=0.20), 1109.07 cm^{-1} (x=0.0), 1109.07 cm^{-1} (x=0.10), 1112.93 cm^{-1} (x=0.15), 1165.00 cm^{-1} (x=0.0), 1381.03 cm^{-1} (x=0.0), 1377.17 cm^{-1} (x=0.10), 1462.04 cm^{-1} (x=0.0), 1479.40 cm^{-1} (x=0.2) at 1100 °C. The abovementioned absorption peaks are appeared due to the deformation of C–H group [36]. The bands around 1629.85 cm^{-1} (x=0.0), 1627.92 cm^{-1} (x=0.10), 1627.92 cm^{-1} (x=0.15), 1625.99 cm^{-1} (x=0.20), 1743.65 cm^{-1} (x=0.0), 2380.41 cm^{-1} (x=0.0), 2380.41 cm^{-1} (x=0.10), 2369.70 cm^{-1} (x=0.15), 2380.41 cm^{-1} (x=0.20), 2854.65 cm^{-1} (x=0.0), 2854.65 cm^{-1} (x=0.20), 2924.09 cm^{-1} (x=0.0), 2926.01 cm^{-1} (x=0.10), 2926.01 cm^{-1} (x=0.15), 2924.09 cm^{-1} (x=0.20), which are attributed due to the stretching and bending vibrations of H–O–H, absorbed water and atmospheric CO_2 [37]. 3444.87 cm^{-1} (x=0.0), 3444.87 cm^{-1} (x=0.10), 3446.79 cm^{-1} (x=0.15), 3437.15 cm^{-1} (x=0.20), 3693.68 cm^{-1} (x=0.0), 3691.75 cm^{-1} (x=0.10), 3695.61 cm^{-1} (x=0.15), 3693.68 cm^{-1} (x=0.20), and 3774.69 cm^{-1} (x=0.0), 3774.69 cm^{-1} (x=0.20), 3776.62 cm^{-1} (x=0.10), 3772.76 (x=0.15), 3876.92 (x=0.20) are attributed due to the presence of small moisture. On the contrary, the following bands appeared in the spectrum such as 1109.07 cm^{-1} (x=0.0), 1109.07 cm^{-1} (x=0.10), 1109.07 cm^{-1} (x=0.15), 1107.12 cm^{-1} (x=0.20), 1163.08 cm^{-1} (x=0.0), 1438.90 cm^{-1} (x=0.0) at 1200 °C. The abovementioned absorption peaks are appeared due to the deformation of C–H group [36]. The bands around 1625.99 (x=0.0), 1624.06 cm^{-1} (x=0.10), 1627.72 cm^{-1} (x=0.15), 1625.99 cm^{-1} (x=0.20), 1749.44 cm^{-1} (x=0.0), 1755.22 cm^{-1} (x=0.10), 1751.36 cm^{-1} (x=0.20), 2380.41 cm^{-1} (x=0.0), 2380.41 cm^{-1} (x=0.10), 2380.41 cm^{-1} (x=0.15), 2380.41 cm^{-1} (x=0.20), 2854.65 cm^{-1} (x=0.0), 2856.58 cm^{-1} (x=0.10), 2856.58 cm^{-1} (x=0.15), 2856.58 cm^{-1} (x=0.20), 2924.09 cm^{-1} (x=0.0), 2922.16 cm^{-1} (x=0.10), 2924.09 cm^{-1} (x=0.15), 2924.09 cm^{-1} (x=0.20), 3437.15 cm^{-1} (x=0.0), 3441.01 cm^{-1} (x=0.10), 3444.87 cm^{-1} (x=0.15), 3435.22 cm^{-1} (x=0.20) which are attributed due to the stretching and bending vibrations of H–O–H, absorbed water and atmospheric CO_2 [37]. 3693.68 cm^{-1} (x=0.0), 3697.64 cm^{-1} (x=0.10), 3693.68 cm^{-1} (x=0.15), 3693.68 cm^{-1} (x=0.20), 3770.84 cm^{-1} (x=0.0), 3770.84 cm^{-1} (x=0.10), 3770.84 cm^{-1} (x=0.15), 3774.69 cm^{-1} (x=0.20), and 3874.99 cm^{-1} (x=0.0), 3876.92 cm^{-1} (x=0.10),

3874.99 cm^{-1} (x = 0.20) are attributed due to the presence of small moisture.

3.3 Microstructural and elemental analysis

Figures 3a–d and 4a–d show typical SEM images and EDAX spectra of $Mg_{0.2-x}Ca_xMn_{0.5}Zn_{0.3}Fe_2O_4$ ferrites sintered at 1100 and 1200 °C. It is clear from SEM images that the $Mg_{0.2}Mn_{0.5}Zn_{0.3}Fe_2O_4$ ferrite consists of some irregularly cubic particles at 1100 and 1200 °C. On the contrary, sharp hexagonal/plate like-shaped stack on each other are formed with the increase of Ca^{2+} concentration at 1100 and 1200 °C. The average grain sizes of the samples sintered at 1100 and 1200 °C is presented in Table 2. It is found that the grain size increases with increasing Ca^{2+} concentrations and it strongly depends on the amount of Ca^{2+}. Ca^{2+} influences the morphology by forming a liquid phase during sintering and expedites the grain growth by lowering the rate of cation interdiffusion [38, 39]. It is also found that the average grain size of the synthesized samples is greater than 2.8 µm for both sintering temperatures, which is assumed to remain in the multi-domain structure [40]. EDAX confirms the presence of Mg^{2+}, Ca^{2+}, Mn^{2+}, Zn^{2+}, Fe^{3+}, and O^{2-} as per the initial stoichiometry.

3.4 Variation of dielectric constant

Figure 5a, b shows frequency dependent real part (ε') of dielectric constant for $Mg_{0.2-x}Ca_xMn_{0.5}Zn_{0.3}Fe_2O_4$ ferrites sintered at 1100 and 1200 °C. It is observed that ε' decreases as frequency increases showing usual dielectric and it remains constant at higher frequencies. The dispersion in dielectric behavior is attributed due to the Maxwell–Wagner [41, 42] interfacial space charge polarization in agreement with Koop's phenomenological theory [43]. The low value of ε' at high frequency is in good agreement with the previous reports [27] and the high value of ε' often at low frequency is due to the effect of heterogeneity of the ferrite samples such as pores, surfaces and layers on grains. It is observed that the value of increases with Ca^{2+} concentration at 1100 and 1200 °C. Figure 5c, d shows the value of ε' as function of Ca^{2+} concentration at different selected frequencies. As the Ca^{2+} concentration is increasing the value of ε' is increasing up to x = 0.10, thereafter, it displayed a decrease on further increasing Ca^{2+} concentration. It is known that Fe^{3+} ions reside on both A and B-sites in $Mg_{0.2}Mn_{0.5}Zn_{0.3}Fe_2O_4$ lattice. After the substitution of Mg^{2+} by Ca^{2+}, some Mg^{2+} ions occupy A-sites in $Mg_{0.2}Mn_{0.5}Zn_{0.3}Fe_2O_4$ lattice and displace Fe^{3+} ions from A-sites. Therefore, the displaced Fe^{3+} ions migrate from A-site to B-site. As a consequence, the concentration of Fe^{3+} at B-site increases and the hopping conduction increases. The probability of occupying Ca^{2+} on A-site is

very rare owing to the larger ionic radius of Ca^{2+} (1.14 Å). Therefore, the substitution of Ca^{2+} enhances the dielectric polarization, consequently the dielectric constant.

3.5 Variation of dielectric loss

Figure 6a, b shows the variation of dielectric loss tangent (tanδ) for $Mg_{0.2-x}Ca_xMn_{0.5}Zn_{0.3}Fe_2O_4$ ferrites with frequency sintered at 1100 and 1200 °C. From the Fig. 6a, b, it is observed that tanδ decreases rapidly at low frequencies is in accordance with the Koop's phenomenological model [43], however, when the frequency increases the rate of decrease in tanδ turns out to be slow and becomes independent of frequency. Generally, tanδ in ferrites is originated electron hopping and charged defect dipoles [44]. In the low frequency domain, tanδ is attributed to electron hopping, while in the high frequency domain; tanδ attributes to the response of the defect dipoles to the field. The defect dipoles are formed due to change in the cation state, such as Fe^{3+}/Fe^{2+}, Mg^{2+}/Mg^{3+}, Zn^{2+}/Zn^{3+} or Mn^{2+}/Mn^{3+}, during the heating process. With the increase of frequency, relaxation of dipoles under the influence of electric field is decreased. As result, tanδ is decreased in the high frequency domain [44]. Furthermore, it is worthwhile to mention that tanδ starts to increase at a frequency of ≥46.6 MHz for x = 0.10 when the sample sintered at 1100 °C. On the contrary, tanδ starts to increase at a frequency of ≥25.03 MHz for x = 0.10, 0.15 and 0.20 when the samples sintered at 1200 °C. At lower frequency region, the value of tanδ is high which is attributed due to the lower conductivity of grain boundary because the more energy is required for electron exchange between $Fe^{2+} \leftrightarrow Fe^{3+}$. In the higher frequency range, tanδ is low which is attributed due to the higher conductivity of grain because the small amount of energy is required for electron transfer between $Fe^{2+} \leftrightarrow Fe^{3+}$ [45]. The x = 0.20 sample exhibits loss peak at a frequency of ≤1 MHz when the sample sintered at 1100 °C. A maximum in tanδ is observed when $\omega\tau = 1$, where ω is the angular frequency of the field ($\omega = 2\pi f_{max}$) and τ is the relaxation time which is inversely proportional to the hopping probability per unit time ($\tau = (1/2)p$)) or $f_{max} = (1/\pi)p$ [46, 47]. The loss is attributed due to the imperfection in crystal lattice and impurities [48]. It is observed that the tanδ increases in the high frequency region with the increase of Ca^{2+} concentration which may be attributed due to the appearance of small pores [49]. Figure 6c, d shows the variation of tanδ as a function of Ca^{2+} concentration at different selected frequencies. As the Ca^{2+} concentration is increasing the tanδ is increasing up to x = 0.10, thereafter, it displayed a decrease with the further increase of Ca^{2+} concentration. The replacement of Mg^{2+} by Ca^{2+} might have been improved the DC resistivity of the ferrites. As a result, the tanδ decreases [50]. The tanδ
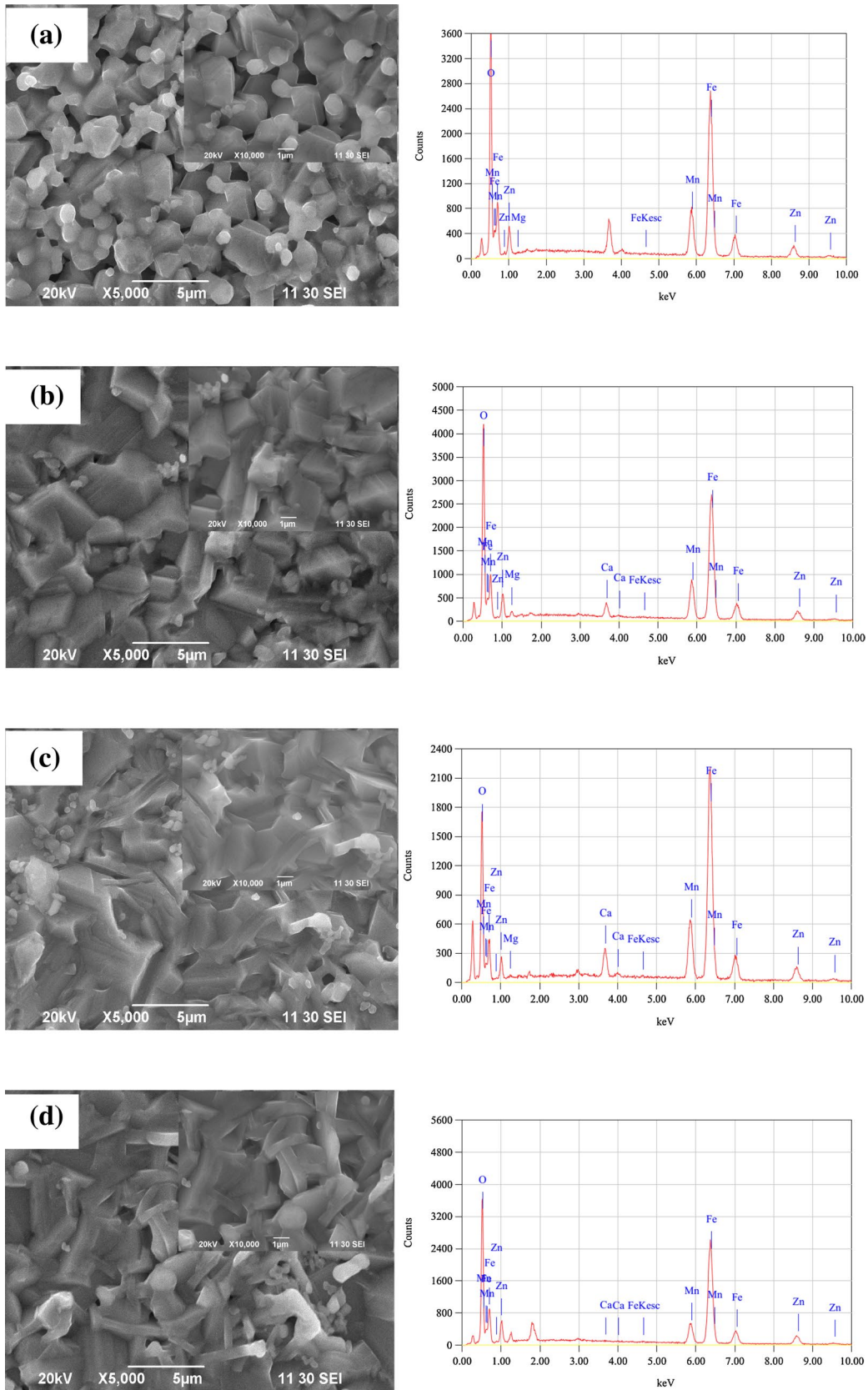
Fig. 3 Typical scanning electron microscopic (SEM) images and EDAX spectra of $Mg_{0.2-x}Ca_xMn_{0.5}Zn_{0.3}Fe_2O_4$ (x = 0.0 0.10, 0.15, and 0.20) ferrite sintered at 1100 °C for 4 h: **a** x = 0.0, **b** x = 0.10, **c** x = 0.15, and **d** x = 0.20, respectively
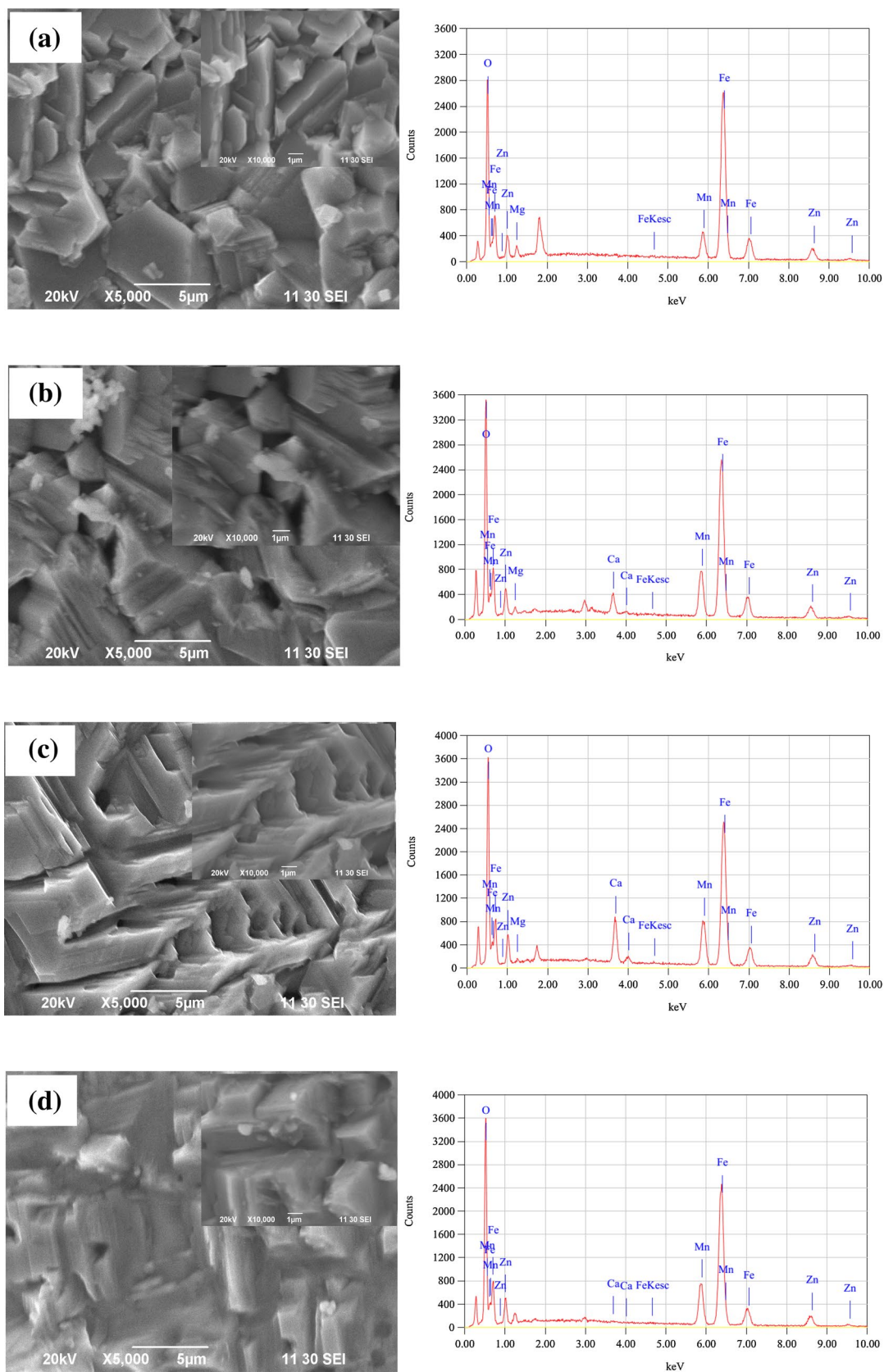
Fig. 4 Typical scanning electron microscopic (SEM) images and EDAX spectra of $Mg_{0.2-x}Ca_xMn_{0.5}Zn_{0.3}Fe_2O_4$ ($x = 0.0$ 0.10, 0.15, and 0.20) ferrite sintered at 1200 °C for 4 h: **a** $x = 0.0$, **b** $x = 0.10$, **c** $x = 0.15$, and **d** $x = 0.20$, respectively
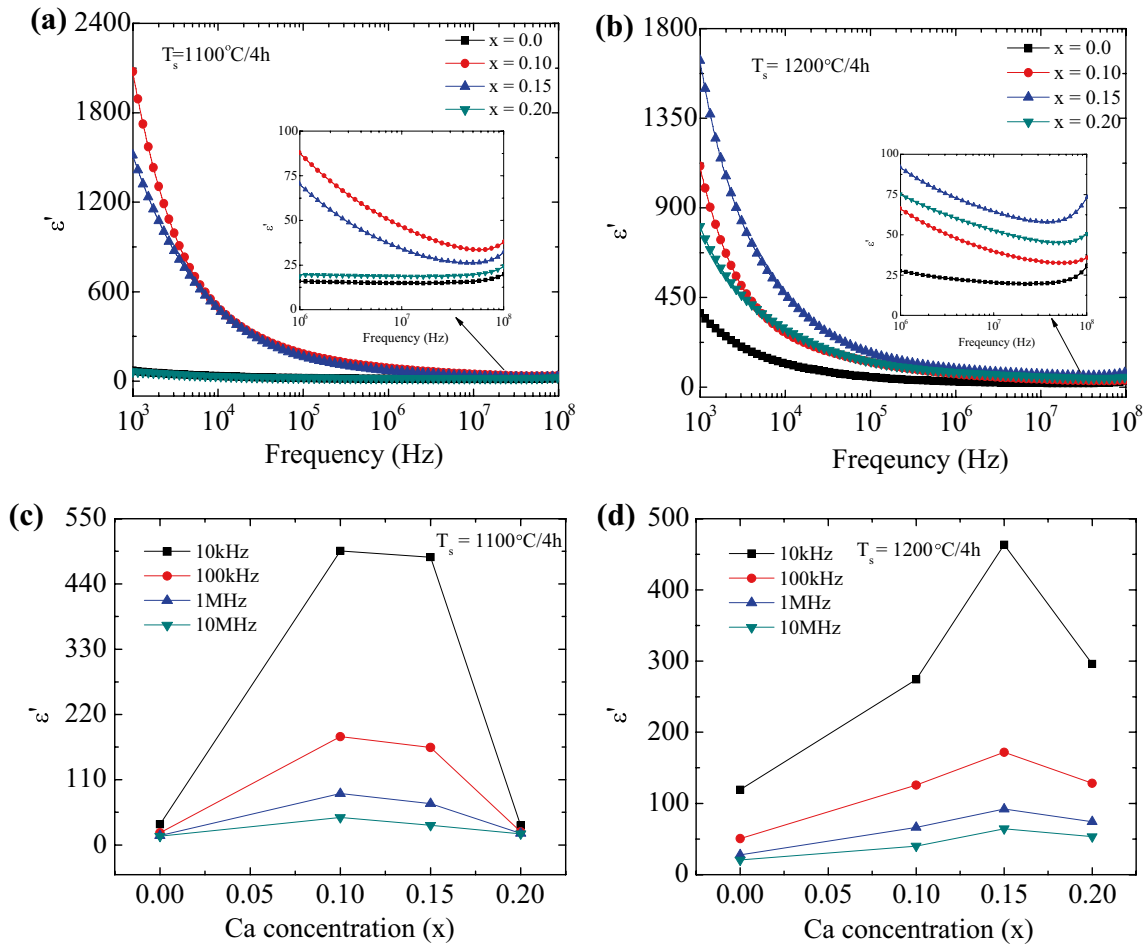
Fig. 5 Variation of the real part (ε') of dielectric constant with frequency of $Mg_{0.2-x}Ca_xMn_{0.5}Zn_{0.3}Fe_2O_4$ ($x = 0.0$ 0.10, 0.15, and 0.20) ferrites sintered at **a** 1100 °C and **b** 1200 °C for 4 h and **c**, **d** composition dependent dielectric constant (ε') at different frequencies

also decreases with increasing Ca^{2+} concentration. As the frequency increases the tanδ increases. This phenomenon could be attributed to the microstructure with poor surface area.

3.6 Variation of ac conductivity

Figure 7a, b shows the variation of ac conductivity (σ_{ac}) for $Mg_{0.2-x}Ca_xMn_{0.5}Zn_{0.3}Fe_2O_4$ ferrites with frequency sintered at 1100 and 1200 °C, respectively. At low frequency region, it is observed that σ_{ac} almost remains constant and it increases in the high frequencies region. The increase in σ_{ac} at the high frequency region is attributed to the enhancement of electron hopping between the charge carriers. Figure 7c, d shows the variation of σ_{ac} as function of Ca^{2+} concentration at different frequencies sintered at 1100 and 1200 °C, respectively. The samples $x = 0.10$ and 0.15 exhibited the highest σ_{ac} at 1100 and 1200 °C. This improvement in σ_{ac} is attributed due to the increase in the charge carrier's with the increases of Ca^{2+} concentration [51]. It was assumed that the Ca^{2+} occupy the A-site [52]. Hence, some Fe^{3+} migrates from the A-site to the B-site. The migration of Fe^{3+} may be accompanied by the formation of Fe^{2+} ions in the B-site [53]. Thus, the ratio Fe^{2+}/Fe^{3+} in the B-site increases which causes the probability of hopping between Fe^{2+}/Fe^{3+} and consequently σ_{ac} increases. A further increase in Ca^{2+} concentration leads to a decrease in σ_{ac}. This decrement in σ_{ac} for high Ca^{2+} may be attributed due to the decreased conduction path as a result of a local distortion of the $Mg_{0.25}Mn_{0.25}Zn_{0.5}Fe_2O_4$ lattice. The source of this distortion may be originated from the difference in the charge and ionic radii between Mg^{2+} and Ca^{2+} cations. The decreasing in σ_{ac} for higher Ca^{2+} concentrations is possibly due to larger formation Fe^{2+} at higher sintering temperature. The magnitude of electron exchange interaction between Fe^{2+} and Fe^{3+} depends on the concentration of Fe^{2+}/Fe^{3+} present on the crystallographically equivalent sites. When the Mg^{2+} is completely replaced by the Ca^{2+}, the σ_{ac} lies between the values of $x = 0.10$ and 0.15 samples. The sample $x = 0.10$ shows the highest electrical
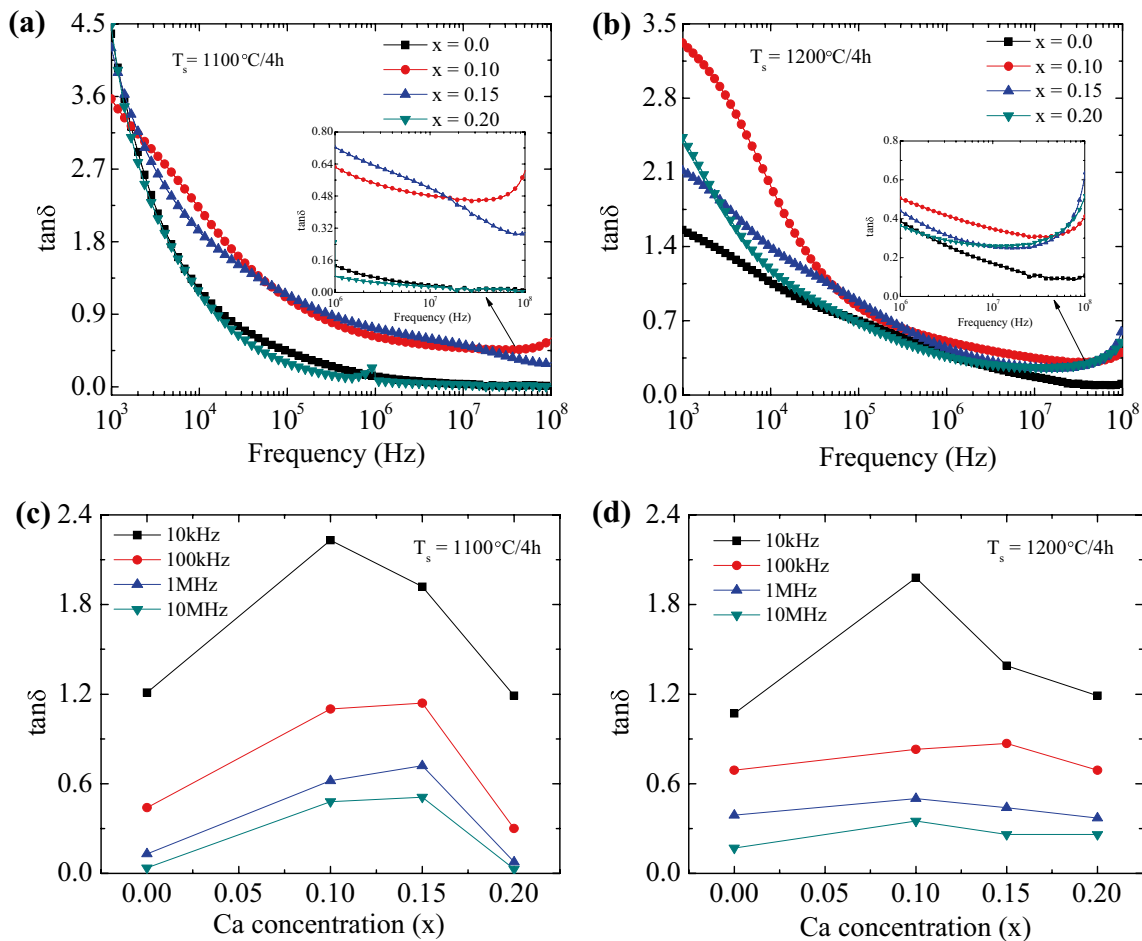
Fig. 6 Variation of dielectric loss (tanδ) with frequency of $Mg_{0.2-x}Ca_xMn_{0.5}Zn_{0.3}Fe_2O_4$ (x = 0.0, 0.10, 0.15, and 0.20) ferrites sintered at **a** 1100 °C and **b** 1200 °C for 4 h and **c**, **d** composition dependent tanδ at different frequencies, respectively

conductivity which is attributed due to the electron hopping between Fe^{3+} and Fe^{2+} increases as the migration of Fe^{3+} to the B-sites increases with increasing the occupancy of Ca^{2+} in the A-sites at 1100 °C [52]. Furthermore, the slight decrease of σ_{ac} for x = 0.15 and 0.20 samples is due to a slight decrease of the electron hopping between Fe^{3+} and Fe^{2+} as a result of migration small fraction of Ca^{2+} to the B-sites.

3.7 Complex impedance spectroscopy

Figure 8a, c shows the variation of real part (Z′) of impedance for $Mg_{0.2-x}Ca_xMn_{0.5}Zn_{0.3}Fe_2O_4$ ferrites sintered at 1100 and 1200 °C. It is seen that Z′ decreases as the frequency increases up to ≤0.1 MHz and attain a constant value at ≥1 MHz. The decrement in Z′ with the increase of frequency indicates that the value of σ_{ac} is enhanced [54]. At high frequency region, the value of Z′ merged together. Therefore, at higher frequency, the merger of curves

indicates the reduction of space charge polarization and a consequently barrier properties of the materials is lowered [55]. Figure 8b, d shows the imaginary part (Z″) of impedance at 1100 and 1200 °C. Samples x = 0.10, 0.15 and 0.20 samples show peak in Z″ and the peak shifts to high frequency region. The shifting of peak to the lower frequency region is attributed to the presence of space charge, which is related to the charge carriers in association with the oxygen vacancies [56, 57]. The peak in Z″ indicates the beginning of electrical relaxation [58].

3.8 Nyquist plots

Nyquist plots of $Mg_{0.2-x}Ca_xMn_{0.5}Zn_{0.3}Fe_2O_4$ ferrites sintered at 1100 and 1200 °C is presented in Fig. 9a, b, respectively. Depending on the grain, grain boundary, and grain-electrode effects three semicircles are appeared in Nyquist plots. The semicircle in low frequency region and the semicircles in the high frequency are attributed due to
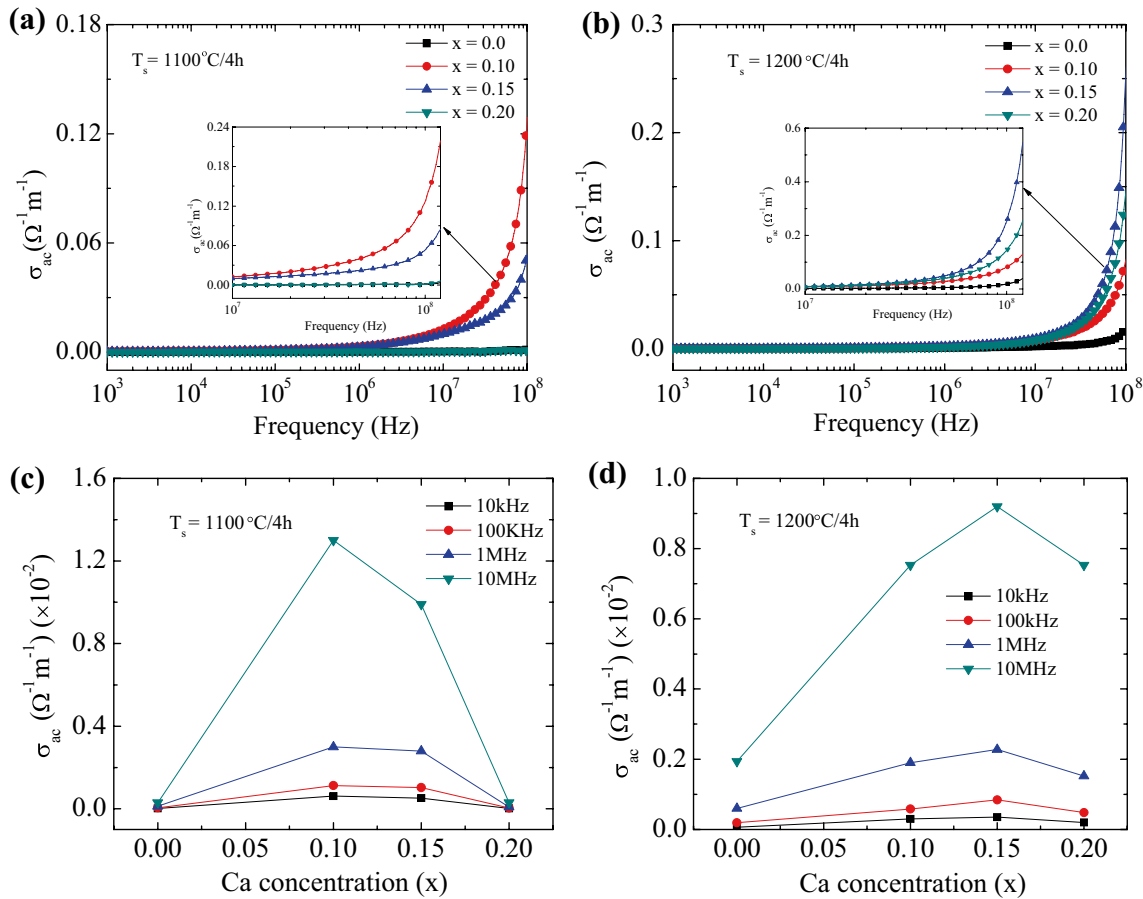
Fig. 7 The variation of ac conductivity (σ_{ac}) as a function of frequency for $Mg_{0.2-x}Ca_xMn_{0.5}Zn_{0.3}Fe_2O_4$ (x = 0.0, 0.1, 0.15, and 0.2) ferrites sintered at: **a** 1100 °C and **b** 1200 °C for 4 h and **c**, **d** composition dependent tanδ at different frequencies, respectively

the grain boundary properties and the grain or bulk property [59]. It is observed that the $Mg_{0.2}Mn_{0.5}Zn_{0.3}Fe_2O_4$ and x = 0.20 samples exhibit single semicircle when the samples sintered at 1100 °C for 4 h. The appearance of the single semicircle in $Mg_{0.2}Mn_{0.5}Zn_{0.3}Fe_2O_4$ at 1100 °C is due to the existence of localized and nonlocalized conduction phenomena. Therefore the conduction process in $Mg_{0.2}Mn_{0.5}Zn_{0.3}Fe_2O_4$ ferrite takes place predominantly through the grain interior only [60]. It is observed that incomplete semicircular arc with large positive slope appears in $Mg_{0.2}Mn_{0.5}Zn_{0.3}Fe_2O_4$ sample at 1200 °C which is due to the very high of impedance. There is a tendency for forming two semicircles. A small semicircle at high frequencies corresponding to grain and large semicircle at low frequencies corresponding to grain boundary effect for x = 0.10 and 0.15 samples at 1100 and 1200 °C, respectively [61]. The sample x = 0.10 exhibits three semicircle at 1100 °C. As the Ca^{2+} concentration increases the diameter of the semicircle decreases except for x = 0.10 which indicates that the grain interior resistance reduces [62].

3.9 Variation of complex permeability

Figure 10 show the real part (μ_i') of complex permeability of $Mg_{0.2-x}Ca_xMn_{0.5}Zn_{0.3}Fe_2O_4$ ferrites sintered at (a) 1100 and (c) 1200 °C. The μ_i' spectra show a complicated variation with the variation of Ca^{2+} concentration at both sintering temperatures. The value of μ_i' for x = 0.10, significantly decreases as compared to that of $Mg_{0.2}Mn_{0.5}Zn_{0.3}Fe_2O_4$ at 1100 °C for 4 h. The value of μ_i' for x = 0.15 is higher than x = 0.10 but it is low as compared to $Mg_{0.2}Mn_{0.5}Zn_{0.3}Fe_2O_4$ which means that the magnetic state of $Mg_{0.2}Mn_{0.5}Zn_{0.3}Fe_2O_4$ is slightly influenced by the presence of Ca^{2+}. When the doping level is less than x = 0.15, the amount of Ca^{2+} appears to be too low to give homogeneous liquid sintering. At x = 0.15, the presence of a few large faceted crystallites gives a higher value of μ_i'. The liquid phase is formed with intragranular porosity at higher Ca^{2+} concentration, and μ_i' decreases. When the Mg^{2+} is completed substituted by the Ca^{2+}, the value of μ_i' is the lowest one as compared to $Mg_{0.2}Mn_{0.5}Zn_{0.3}Fe_2O_4$ sample. The sample x = 0.10 exhibits the minimum value of μ_i' at
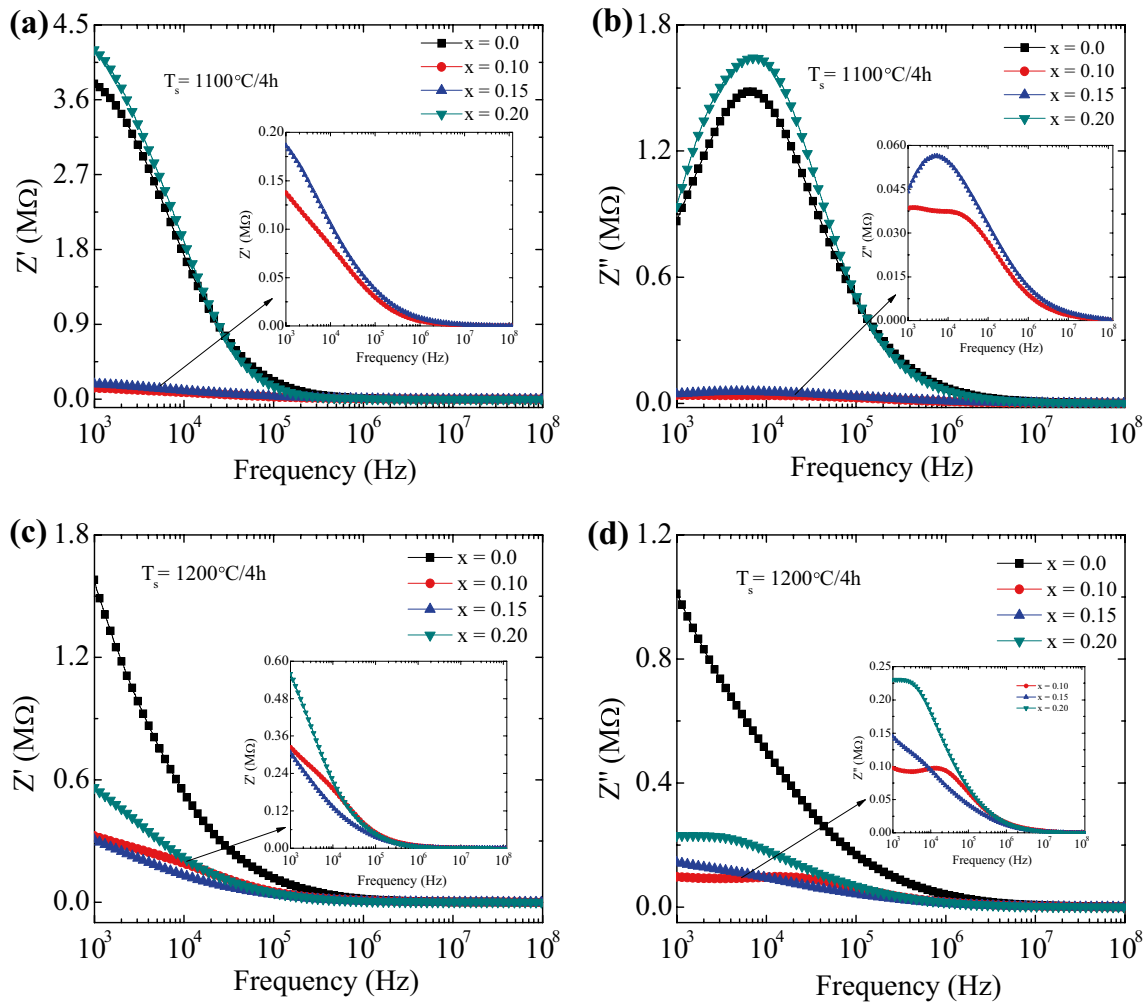
Fig. 8 Variation of real part of impedance (Z') and imaginary part of impedance (Z'') with frequency of $Mg_{0.2-x}Ca_xMn_{0.5}Zn_{0.3}Fe_2O_4$ ($x = 0.0$ 0.10, 0.15, and 0.20) ferrites **a**, **b** sintered at 1100 °C and **c**, **d** sintered at 1200 °C for 4 h, respectively

1200 °C. The value of μ'_i for x = 0.15 substantially decreases as compared to that of $Mg_{0.2}Mn_{0.5}Zn_{0.3}Fe_2O_4$ ferrite. But the value of μ'_i for x = 0.15 is higher than that of x = 0.10 but it is low as compared to that of $Mg_{0.2}Mn_{0.5}Zn_{0.3}Fe_2O_4$. When the Mg^{2+} is completed replaced by the Ca^{2+}, the value of μ'_i is the lowest one as compared to that of x = 0.10 and x = 0.15. In general, complex permeability of polycrystalline ferrites is strongly dependent on grain size, porosity etc. [63]. It is well know that the permeability of polycrystalline ferrites is the combined effect spin rotation and domain wall motion. At low frequency, the contribution of spin rotation is smaller than domain wall motion which is due to the reversible motion of domain walls in the case of a weak magnetic field [63]. The contribution of domain wall motion is negligible at low frequency [64, 65]. The μ'_i for polycrystalline ferrite due to the domain wall motion can be delineated as.

$$(\mu'_i)_{DW} = 1 + \frac{3M_s^2 D}{16\gamma_{DW}}$$

where M_s is the saturation magnetization, D the average grain diameter, and γ_{DW} the domain wall energy [66]. It is observed that the μ'_i remains constant up to a certain frequency called resonance frequency, and then exhibits a shallow peak before falling to low value for $Mg_{0.2}Mn_{0.5}Zn_{0.3}Fe_2O_4$ sample when the sample sintered at 1100 and 1200 °C [67]. It is observed that μ'_i remains constant up to a certain frequency and then falling rapidly to relatively low values for x = 0.10, 0.15 and 0.20, respectively. It is also observed that the natural resonance peak gradually disappears for the Ca^{2+} substituted samples, which exhibits excellent higher frequency properties of the ferrites. It is found that the value of μ'_i significantly reduces with the increases of Ca^{2+} concentration
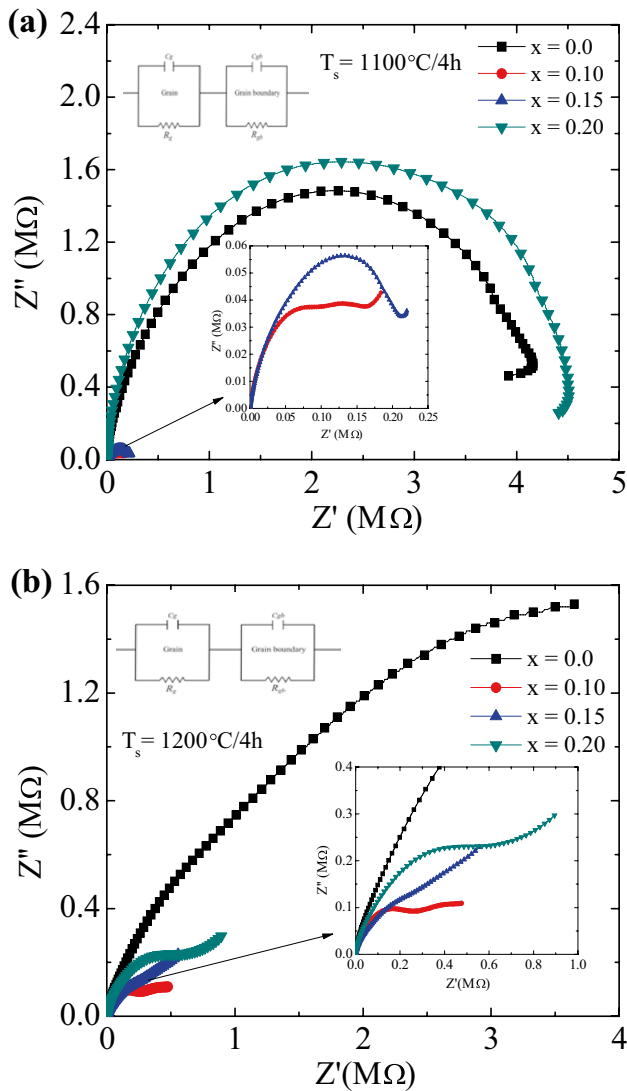
Fig. 9 Cole–Cole plot of impedance of $Mg_{0.2-x}Ca_xMn_{0.5}Zn_{0.3}Fe_2O_4$ (x = 0.0 0.10, 0.15, and 0.20) ferrites sintered at **a** 1100 °C and **b** 1200 °C for 4 h, respectively

crystalline anisotropy which results in the decrease of μ'_i to a smaller value than that of the sample without Ca^{2+} [19]. For a higher amount of Ca^{2+}, the decrease of the magnetization and μ'_i, as well as the increase of the resistivity suggest that Ca^{2+} are dissolved in $Mg_{0.2}Mn_{0.5}Zn_{0.3}Fe_2O_4$ lattice beyond their solubility limit; secondary phases $Ca_2Fe_2O_5$ and $CaFe_2O_4$ with magnetically compensated sublattices appear at the boundaries. At the same time, the segregation process is enhanced with increasing Ca^{2+} concentration, resulting in a depletion of the ferromagnetic phase in Ca^{2+}. Apart from the reduction in saturation magnetization, the value of μ'_i for $Mg_{0.2}Mn_{0.5}Zn_{0.3}Fe_2O_4$ ferrite with the increase of Ca^{2+} concentration may be partly due to the presence of a $Ca_2Fe_2O_5$ and $CaFe_2O_4$ compound [19, 21, 24]. The value of μ'_i at 1200 °C is much better than that of 1100 °C which is attributed due to the increased grain size [71] as well as the decrement of magnetic anisotropy. Magnetic anisotropy decreases due to the reduction of the internal stresses and crystal anisotropy when the sintering temperature increases [72]. The decrement of magnetic anisotropy may results minimum impediment for the domain walls motion. So that μ'_i increases with increase in sintering temperature. The values of μ'_i the samples at a particular frequencies sintered at different temperatures are shown in Table 3. Figure 10b, d shows the variation of magnetic loss (tanδ) with frequency at 1100 and 1200 °C. The tanδ arises due to the lag of domain walls motion with respect to the applied alternating magnetic field and imperfections in the synthesized ferrite lattice [73]. The values of tanδ are observed to decrease initially with frequency ($\leq 10^5$ Hz), reaching a minimum value (≤ 1), and then become almost constant up to 1 MHz. The value of tanδ decreases with increasing frequency because the domain wall motion cannot follow the applied field at a certain frequency. The increase in tanδ at ≥ 1 MHz indicates that the beginning of a possible resonance [74]. When the resonance occurs, there is a rapid increase in tanδ because the maximum energy is transferred from the applied field to the lattice. It is clear from Fig. 10b, d that the tanδ at 1200 °C is higher than that of 1100 °C which is attributed due to the increased Zn^{2+} loss. The loss of Zn^{2+} creates defects in the synthesized samples lattice. The values of tanδ of the samples at a particular frequencies sintered at different temperatures are presented in Table 3.

3.10 Relative quality factor

Figure 11a, b shows the relative quality factor (RQF) for $Mg_{0.2-x}Ca_xMn_{0.5}Zn_{0.3}Fe_2O_4$ ferrites as function of frequency sintered at 1100 and 1200 °C. From Fig. 11a, b, it is observed that RQF shows a peak at particular frequencies for both sintering temperature. The peak values of RQF shows exactly similar behaviour to that of μ'_i since
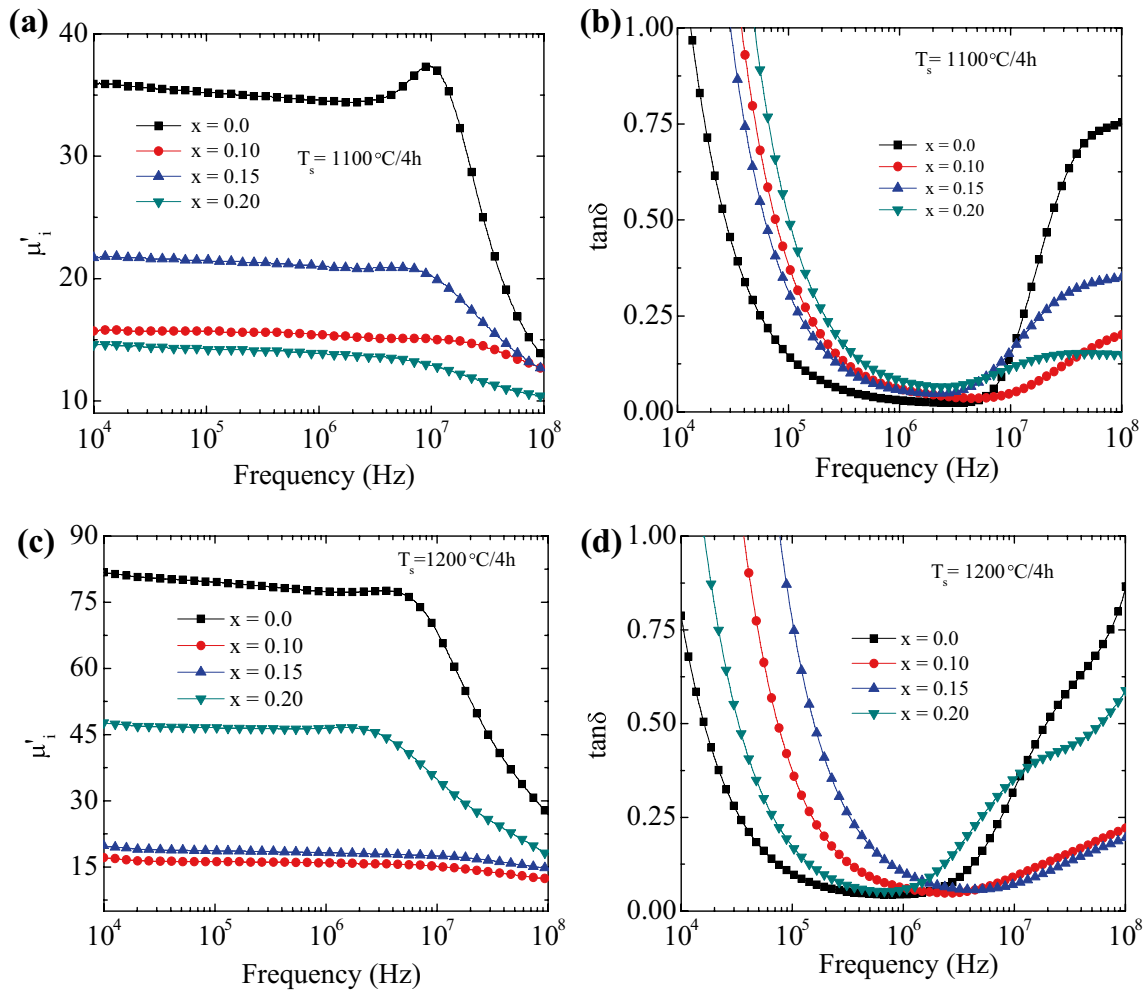
for both sintering temperature which is attributed due to lower saturation magnetization and increased inner stress or magneto crystalline anisotropy. When Ca^{2+} entered the $Mg_{0.2}Mn_{0.5}Zn_{0.3}Fe_2O_4$ lattice; it forced a larger fraction of Fe^{3+} to occupy B-sites. Therefore, the magnetic dilution of the A-sites increases. The A-site to B-site interaction is much weaker than the B-site to B-site interaction when the concentration of Ca^{2+} on A-sites increased to a certain value. Therefore, the weakened interaction between the B-site and A-site lattices divides B-site lattice into two sublattices with a canted magnetic moment, which expedites the decrease in the saturation magnetization [25, 68, 69]. Due to the intragranular pores magnetic properties deteriorates [70]. The intragranular pores pin the domain walls motion. Moreover, the Ca^{2+} induces an increase of the

Fig. 10 Variation of real part of permeability (μ_i') and magnetic loss (tanδ) with frequency of $Mg_{0.2-x}Ca_xMn_{0.5}Zn_{0.3}Fe_2O_4$ (x = 0, 0.10, 0.15, and 0.20) ferrites: **a**, **b** sintered at 1100 °C and **c**, **d** sintered at 1200 °C for 4 h, respectively

Table 3 Initial permeability (μ'), magnetic loss (tanδ) and RQF at different selected frequencies and maximum RQF ((RQF)max) for $Mg_{0.2-x}Ca_xMn_{0.5}Zn_{0.3}Fe_2O_4$ (x = 0, 0.10, 0.15, and 0.20) sintered at different sintering temperatures (T_s) for 4h

T_s (°C)	Composition (x)	μ_i' at		tanδ at		RQF at		(RQF)$_{max}$
		1 MHz	10 MHz	1 MHz	10 MHz	1 MHz	10 MHz	
1100	0.0	34.53	37.39	0.030	0.154	1141.24	250.94	1464.32
	0.10	15.44	15.13	0.059	0.049	257.30	310.47	431.75
	0.15	20.92	20.21	0.056	0.160	370.42	127.99	424.13
	0.20	14.01	12.99	0.083	0.117	168.66	112.00	209.58
1200	0.0	77.55	68.63	0.044	0.330	1750.25	208.33	1774.54
	0.10	15.68	15.13	0.060	0.093	258.08	163.98	888.62
	0.15	17.91	17.36	0.103	0.070	176.76	243.37	313.82
	0.20	46.62	34.63	0.057	0.356	818.33	98.05	326.67

it is proportional to the RQF. It is seen that RQF deteriorates beyond 1 MHz for both sintering temperatures, i.e., the tanδ is minimum up to 1 MHz, and then it rises rapidly for all synthesized simples. Deterioration of RQF is clearly observed with the increase of sintering temperature.

The maximum value of RQF for $Mg_{0.2}Mn_{0.5}Zn_{0.3}Fe_2O_4$ is obtained sintered at 1100 and 1200 °C which is probably attributed due to the growth of less imperfections and defects sintered at relatively lower sintering temperature [74]. It is observed that the maximum value of RQF
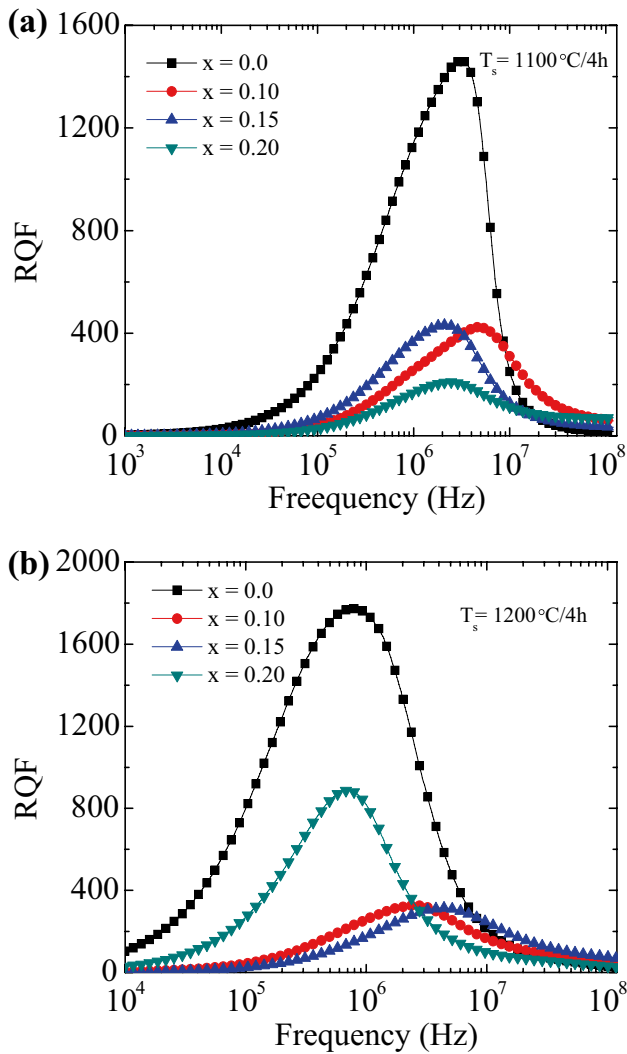
Fig. 11 Variation of relative quality factor (RQF) with frequency of $Mg_{0.2-x}Ca_xMn_{0.5}Zn_{0.3}Fe_2O_4$ (x=0, 0.10, 0.15, and 0.20) ferrites sintered at: **a** 1100 °C and **b** 1200 °C for 4 h, respectively

decreases with the increase of Ca^{2+} concentration. The lower RQF for Ca^{2+} substituted $Mg_{0.2}Mn_{0.5}Zn_{0.3}Fe_2O_4$ ferrites might be due to higher hysteresis loss, which might arise from its porous structure. The decrement in maximum RQF is probably attributed to increase in tanδ [73]. The peak in RQF shifts to higher frequency range for x=0.10 and for x=0.15 and 0.20 shift to the lower frequency range with respect to $Mg_{0.2}Mn_{0.5}Zn_{0.3}Fe_2O_4$ sample when the samples sintered at 1100 °C for 4 h. For x=0.10 and 0.15 samples, RQF shifts to higher frequency domain and on the contrary, RQF shifts to the lower frequency domain for x=0.20 with respect to $Mg_{0.2}Mn_{0.5}Zn_{0.3}Fe_2O_4$ at 1200 °C. The x=0.20 sample exhibits the highest RQF as compared to that of x=0.10 and 0.15 samples at 1200 °C. This improvement in RQF is attributed due to the increased electrical resistivity. It is also seen that RQF is higher at 1200 °C than that of at

1100 °C. The maximum RQF values for the samples sintered at different temperatures are tabulated in Table 3.

4 Conclusions

In the present investigation, we have successfully synthesized Mg–Ca–Mn–Zn ferrites by solid state sintering at 1100 and 1200 °C. XRD and FTIR analyses revealed that the samples are found to be formed spinel phase. The lattice parameter increased due to the difference of ions radius between Mg^{2+} and Ca^{2+}. The SEM images revealed that the average grain size increases with Ca^{2+} which may be attributed due to the fact that Ca^{2+} influences the microstructure by forming a liquid phase during sintering process and expedites the grain growth by lowering the rate of cation interdiffusion. The EDAX spectra confirm the presence of all elements as per initial stoichiometry. Low frequency dielectric dispersion is attributed to the Maxwell–Wagner model and Koops phenomenological theory. Permittivity increases with Ca^{2+} concentration at 1100 and 1200 °C. The samples x=0.10 and 0.15 exhibits highest conductivity at 1100 and 1200 °C, respectively because the electron hopping between Fe^{3+} and Fe^{2+} ions increases. Complex impedance study indicates that the conduction process is due to the grain and grain boundary effect only. Permeability reduces significantly with the increase of Ca^{2+} because Ca^{2+} reduces the saturation magnetization as well as increases the inner stress or crystal magnetic anisotropy. Finally, it can be said that Ca^{2+} substitution effectively tunes the structural, microstructural and electromagnetic properties of $Mg_{0.2}Mn_{0.5}Zn_{0.3}Fe_2O_4$ ferrite.

References

1. O.M. Hemeda, N.Y. Mostafa, O.H.Abd. Elkader, M.A. Ahmed, J. Magn. Magn. Mater. **364**, 39–46 (2014)
2. R. Valenzuela, Phys. Res. Int. **2012**, 1–9 (2012)
3. N.M. Deraz, A. Alarifi, S.A. Shaban, J. Saudi Chem. Soc. **14**, 357–362 (2010)
4. A. Goldman, *Handbook of Modern Ferromagnetic Materials.* (Kluwer Academic Publishers, Boston, 1999)
5. J. Fan, F.R. Sale, J. Eur. Ceram. Soc. **20**, 2743–2751 (2000)
6. Z. Pedzich, M.M. Bucko, M. Krolikowski, M. Bakalarska, J. Babiarz, J. Eur. Ceram. Soc. **24**, 1053–1056 (2004)
7. N.M. Deraz, A. Alarifi, Int. J. Electrochem. Sci. **7**, 6501–6511 (2012)

8. H. Mohseni, H. Shokrollahi, I. Sharifi, Kh. Gheisari, J. Magn. Magn. Mater. **324**, 3741–3747 (2012)

9. U.R. Ghodake, N.D. Chaudhari, R.C. Kambale, J.Y. Patil, S.S. Suryavanshi, J. Magn. Magn. Mater. **407**, 60–68 (2016)

10. H. Rikukawa, U. Kihara, M. Torii, IEEE Trans. Magn. **18**, 1538–1540 (1982)

11. S.S. Gorelik, B.E. Levin, L.M. Letyuk, A.P. Nikol'skii, Sov. Phys. J. **10**, 14–17 (1967)

12. S.A.S. Ebrahimi, Z.P. Fard, Key Eng. Mater. **336–338**, 699–702 (2007)

13. J. Fan, W. Li, H. Zhao, X. Zhang, Z. Zhang, Adv. Mater. Res. **680**, 31–34 (2013)

14. M. Kolenbrander, P. Van Der Zaag, J. de Phys. IV Coll. **07**(C1), C1-195–C1-196 (1997)

15. P.J. van der Zaag, M. Kolenbrander, M.Th. Rekveldt, J. Appl. Phys. **83**, 6870–6872 (1998)

16. B.D. Prasad, H. Nagabhushana, K. Thyagarajan, B.M. Nagabhushana, D.M. Jnaneshwara, S.C. Sharma, C. Shivakumara, N.O. Gopal, S.C. Ke, R.P.S. Chakradhar, J. Magn. Magn. Mater. **358–359**, 132–141 (2014)

17. P.P. Hankare, S.D. Jadhav, U.B. Sankpal, S.S. Chavan, K.J. Waghmare, B.K. Chougule, J. Alloys Compd. **475**, 926–929 (2009)

18. V.G. Harris, A. Geiler, Y.J. Chen, S.D. Yoon, M.Z. Wu, A. Yang, Z.H. Chen, P. He, P.V. Parimi, X. Zuo, C.E. Patton, M. Abe, O. Acher, C. Vittoria, J. Magn. Magn. Mater. **321**, 2035–2047 (2009)

19. C. Pasnicu, D. Condtjracre, E. Luca, Phys. Status Solidi (a) **76**, 145–150 (1983)

20. S.D. Chhaya, M.P. Pandya, M.C. Chhantbar, K.B. Modi, G.J. Baldha, H.H. Joshi, J. Alloys Compd. **377**, 155–161 (2004)

21. S.F. Wang, Y.F. Hsu, Y.X. Liu, C.K. Hsieh, J. Magn. Magn. Mater. **394**, 470–476 (2015)

22. E. Rezlescu, L. Sachelarie, P.D. Popa, N. Rezlescu, IEEE Trans. Magn. **36**, 3962–3967 (2000)

23. R. Ali, M.A. Khan, A. Mahmood, A.H. Chughtai, A. Sultan, M. Shahid, M. Ishaq, M.F. Warsi, Ceram. Int. **40**, 3841–3846 (2014)

24. H. Hirazawa, S. Kusamoto, H. Aono, T. Naohara, K. Mori, Y. Hattori, T. Maehara, Y. Watanabe, J. Alloys Compd. **461**, 467–473 (2008)

25. H.M. Zaki, S.A. Heniti, J. Nanosci. Nanotech. **12**, 7126–7131(2012)

26. A.M. Escamilla-Pérez, D.A. Cortés-Hernández, J.M. Almanza-Robles, D. Mantovani, P. Chevallier, J. Magn. Magn. Mater. **374**, 474–478 (2015)

27. Md.D. Rahaman, Md. Dalim Mia, M.N.I. Khan, A.K.M. Akther Hossain, J. Magn. Magn. Mater. **404**, 238–249 (2016)

28. H.E. Scherrer, H. Kisker, H. Kronmuller, R. Wurschum, Nanostruct. Mater. **6**, 533–538 (1995)

29. B.D. Cullity, *Elements of X-ray Diffraction* (Addison Wesley Publ. Co. Inc., Reading, 1956), p. 42

30. M. Junaid, M.A. Khan, F. Iqbal, G. Murtaza, M.N. Akhtar, M. Ahmad, I. Shakir, M.F. Warsi, J. Magn. Magn. Mater. **419**, 338–344 (2016)

31. Z. Karimi, Y. Mohammadifar, H. Shokrollahi, Sh. Khameneh Asl, Gh. Yousefi, L. Karimi, J. Magn. Magn. Mater. **361**, 150–156 (2014)

32. M.A. Amer, M. El Hiti, J. Magn. Magn. Mater. **234**, 118–125 (2001)

33. K. Standley, *Oxide Magnetic Materials* (Clarendon, Oxford, 1974), p. 97

34. J.R. Macdonald, E. Barsoukov, *Impedance Spectroscopy: Theory, Experiment and Applications*, 2nd edn. (Wiley, Hoboken, 2005)

35. R.D. Waldron, Phys. Rev. **99**, 1727–1735 (1955)

36. B.J. Evans, S. Hafner, J. Phys. Chem. Solids **29**, 1573–1588 (1968)

37. M.G. Naseri, E.B. Saion, H.A. Ahangar, A.H. Shaari, M. Hashim, J. Nanomater. **2010**, 907686 (2010)

38. T. Tsutaoka, J. Appl. Phys. **93**, 2789–2798 (2003)

39. R.L. Coble, T.K. Gupta, in *Sintering and Related Phenomena*, ed. by G.C. Kuczynski, C.F. Gibbon (Gordon & Breach, New York, 1967), p. 423

40. P.J. van der Zaag, P.J. van der Valk, M.Th. Rekveldt, Appl. Phys. Lett. **69**, 2927–2929 (1996)

41. J.C. Maxwell, *Electricity and Magnetism*, (Oxford University Press, London, 1873), p. 328

42. K.W. Wagner, Am. Phys. **40**, 817–855 (1913)

43. C.G. Koops, Phys. Rev. **83**, 121–124 (1953)

44. S.N. Dolia, P.K. Sharma, M.S. Dhawan, S. Kumar, A.S. Prasad, A. Samariya, S.P. Pareek, R.K. Singhal, K. Asokan, Y.T. Xing, M. Alzamora, E. Saitovitach, Appl. Surf. Sci. **258**, 4207–4211 (2012)

45. M.R. Bhandare, H.V. Jamadar, A.T. Pathan, B.K. Chougule, A.M. Shaikh, J. Alloys Compd. **509**, L113–L118 (2011)

46. A.A. Birajdar, S.E. Shirsath, R.H. Kadam, S.M. Patange, D.R. Mane, A.R. Shitre, Ceram. Int. **38**, 2963–2970 (2012)

47. S. Bhagawat, P. Rao, J. Appl. Phys. **3**, 1–6 (2013)

48. J. Rout, R. Choudhary, S. Shannigrahi, H. Sharma, J. Electron. Mater. **44**, 3811–3818 (2015)

49. S. Rasheed, H.S. Aziz, R.A. Khan, A.M. Khan, A. Rahim, J. Nisar, S.M. Shah, F. Iqbal, A.R. Khan, Ceram. Int. **42**, 3666–3672 (2016)

50. Q. Xia, H. Su, T. Zhang, J. Li, G. Shen, H. Zhang, X. Tang, J. Appl. Phys. **112**, 043915 (2012)

51. S. Mollah, K. Som, K. Bose, B.K. Chaudhuri, J. Appl. Phys. **74**, 931–937 (1993)

52. R. Andoulsi, K.H. Naifer, M. Ferid, Ceram. Int. **39**, 6527–6531 (2013)

53. A.A. Sattar, H.M. El-Sayed, W.R. Agami, J. Mater. Eng. Perform. **16**, 573–577 (2007)

54. S.T. Assar, H.F. Abosheiasha, J. Magn. Magn. Mater. **374**, 264–272 (2015)

55. K.M. Batoo, Physica B **406**, 382–387 (2011)

56. A. Kumar, B. Singh, R. Choudhary, A.K. Thakur, Mater. Chem. Phys. **99**, 150–159 (2006)

57. K.M. Batoo, J. Phys. Chem. Solids **72**, 1400–1407 (2011)

58. B. Tiwari, R. Choudhary, J. Alloys Compd. **493**, 1–10 (2010)

59. M.A. Rahman, A.K.M. Akther Hossain, Phys. Scr. **89**, 8 (2014)

60. K.M. Batoo, M.S. Ansari, Nanoscale Res. Lett. **7**, 112–126 (2012)

61. J.R. Macdonald, *Impedance Spectroscopy Emphasizing Solid Materials and System*, 3rd edn. (Wiley, New York, 1987)

62. R.S. Devan, Y.D. Kolekar, B.K. Chougule, J. Phys. **18**, 9809–9821 (2006)

63. A. Goldman, *Modern Ferrite Technology*, (Marcel Dekker Inc., New York, 1993)

64. A. Globus, P. Duplex, IEEE Trans. Magn. **2**, 441–445 (1966)

65. T.Y. Byun, S.C. Byeon, K.S. Hong, IEEE Trans. Magn. **35**, 3445–3447 (1999)

66. A. Globus, P. Duplex, M. Guyd, IEEE Trans. Magn. **7**, 617–622 (1971)

67. N. Bloembergen, Proc. IRE **44**, 1259–1269 (1956)

68. K. Praveena, K. Sadhana, R. Sandhya, S.R. Murthy, H.L. Liu, Ceram. Int. **42**, 8869–8877 (2016)

69. G.K. Joshi, A.Y. Khot, S.R. Sawant, Solid State Commun. **65**, 1593–1595 (1988)

70. A.K.M. Akther Hossain, T.S. Biswas, S.T. Mahmud, T. Yanagida, H. Tanaka, T. Kawai, J. Magn. Magn. Mater. **321**, 81–87 (2009)

71. A. Beitollani, M. Hoor, J. Mater. Sci. **14**, 477–482 (2003)

72. A. Verma, T.C. Goel, R.G. Mendiratta, J. Magn. Magn. Mater. **210**, 274–278 (2010)

73. A.K. Singh, T.C. Goel, R.G. Mendiratta, O.P. Thakur, C. Prakash, J. Appl. Phys. **92**, 3872–3876 (2002)

74. A.K.M. Akther Hossain, M.L. Rahman, J. Magn. Magn. Mater. **323**, 1954–1962 (2011)